LA-UR- 00-5208

Approved for public release; distribution is unlimited.

Title:	SIMULATIONS OF FLOW AROUND A CUBICAL BUILDING: COMPARISON WITH TOWING-TANK DATA AND ASSESSMENT OF RADIATIVELY-INDUCED THERMAL EFFECTS
Author(s):	William S. Smith, Jon M. Reisner, and C.-Y. J. Kao
Submitted to:	Atmospheric Environment, February, 2001

Los Alamos

National Laboratory

Simulations of Flow Around a Cubical Building: Comparison with Towing-Tank Data and Assessment of Radiatively-Induced Thermal Effects

by

W. S. Smith*, J. M. Reisner, and C.-Y. J. Kao

Earth and Environmental Sciences Division

Los Alamos National Laboratory

Los Alamos, NM 87545

For submittal to Atmospheric Environment

(Revised Version)

February, 2001

* Dr. William S. Smith, Earth and Environmental Sciences, Atmospheric and Climate Sciences Group (EES-8), Los Alamos National Laboratory, Los Alamos, New Mexico, USA. 87545, E-mail: wss@lanl.gov

AUTHOR ADDRESSES:

Dr. William S. Smith
Earth and Environmental Sciences
Atmospheric and Climate Sciences Group (EES-8) MS D-401
Los Alamos National Laboratory
Los Alamos, New Mexico, USA. 87545
E-mail: wss@lanl.gov
Telephone: (505) 667-0179

Dr. Jon M. Reisner
Earth and Environmental Sciences
Atmospheric and Climate Sciences Group (EES-8) MS D-401
Los Alamos National Laboratory
Los Alamos, New Mexico, USA. 87545
E-mail: reisner@lanl.gov

Dr. C.-Y. Jim Kao
Earth and Environmental Sciences
Atmospheric and Climate Sciences Group (EES-8) MS C-323
Los Alamos National Laboratory
Los Alamos, New Mexico, USA. 87545
E-mail: kao@lanl.gov

ABSTRACT

A three-dimensional (3-D) computational fluid dynamics (CFD) model, coupled with a meteorological radiation and surface physics package, is used to model the mean flow field and tracer dispersion in the vicinity of an idealized cubical building. We first compare the simulations with earlier numerical studies as well as towing-tank laboratory experiments, where radiation effects were not included. Our simulations capture most of the features revealed by the towing-tank data, including the variation of the flow reattachment point as a function of Froude number and the induction of a prominent lee wave in the low Froude number regime. The simulated tracer concentration also compares very favorably with the data.

We then assess the thermal effects due to radiative heating on the ground and building including shading by the building, on the mean flow and tracer dispersion. Our simulations show that convergence within and beyond the cavity zone causes a substantial lofting of the air mass downstream from the building. This lofting results from the combination of thermal heating of the ground and building roof, and vortex circulation associated with the horseshoe eddy along the lateral sides of the building. The specific effect of shading on the flow field is isolated by comparing simulations for which the radiative heating and shading patterns are kept constant, but the environmental wind direction is altered. It is found that the shading exerts local cooling, which can be combined into the overall thermodynamic interaction, described above, to effectively alter the circulation downstream from the building.

KEY WORDS INDEX:

Large Eddy Simulation
Dispersion
Transport
Urban
Building
Thermal effects

1. INTRODUCTION

There have been numerous three-dimensional (3-D) modeling studies on the flow field around buildings. The first 3-D large eddy simulation (LES) study of the flow around isolated buildings was attempted by Murakami *et al.* (1987). Dawson *et al*. (1991) used the TEMPEST code (Trent and Eyler, 1983) with a $k-\varepsilon$ closure to simulate the data from wind tunnel experiments of flow around a 3-D cubical obstacle (Thompson and Lombardi, 1977). Zhang *et al*. (1993; 1996) also used TEMPEST to perform 3-D simulations of flow and dispersion around an isolated cubical building and compare their results with towing tank data obtained from the USEPA (U. S. Environmental Protection Agency, Snyder, 1994). Guenther *et al*. (1990) used the CELESTE code (a derivative of TEMPEST) to simulate the flow field in an industrial complex with multiple buildings in a wintertime Arctic boundary layer where the solar insolation is negligible.

3-D studies of radiative heating and shadowing effects on the flow and dispersion around buildings have rarely been attempted in the literature probably due to the required computational resources and the lack of experimental data. Radiative heating and cooling can introduce significant thermal effects on the atmospheric stability within the atmospheric boundary layer. Direct heating and shadowing associated with the atmospheric short-wave radiation due to buildings in an urban environment can further impact the dynamical flow and dispersion through thermally induced eddies. Much of the literature addressing such effects has focused on the urban street canyons, whose geometry is essentially two-dimensional (2-D) in nature. For example, Sini *et al*. (1996) and Mestayer *et al*. (1995) used a CFD model with standard $k-\varepsilon$ closure to show that thermal heating on the downstream wall of a street canyon can result in counter-rotating vortices within the street canyon. This results in a reduced vertical exchange of pollutants near the pedestrian level of the street canyon due to multi-vortex flow splitting.

An earlier study by Reisner *et al*. (1998) used the same 3-D CFD code used in the present study, coupled with a physical package consisting of a longwave and shortwave radiative treatment and a ground surface parameterization, to simulate the effect of radiative heating on the flow field and tracer evolution in the vicinity of an urban mall environment encompassing about 40 buildings. The results showed that the inclusion of radiative heating effects during an early afternoon tracer release can result in the tracer being swept up into the boundary layer by thermal eddies. Due to a lack of experimental data, our earlier study (Reisner *et al*., 1998) is not considered conclusive. But, it warrants a closer look at the radiatively induced thermal effects due to buildings.

In this paper, the validity of our CFD code without radiative effects is first examined by comparing a number of model simulations with an earlier water tank study and associated numerical simulations for flow around an idealized cubical building. We then carefully examine the effects of surface heating and shadowing on the dynamical flow field in the vicinity of an idealized cubical block, and the corresponding tracer evolution. Section 2 of this paper briefly describes the CFD model and physics package used in this study. Section 3 presents a validation of results of our simulations against towing-tank data, while section 4 presents results due to radiative heating. Concluding remarks are given in section 5.

2. MODEL

2.1. *Model Dynamics*

The model used for this study is based on the approach described Smolarkiewicz and Margolin (1993). This model has been undergoing extensive testing and development at Los Alamos National Laboratory in order to meet the modeling requirements of the Department of Energy Chemical and Biological Weapons Nonproliferation Program (DOE CBNP). The numerical integration is second order accurate in space and time, and based on a nonoscillatory forward-in-time advection scheme (MPDATA, see Smolarkiewicz and Margolin, 1998). It has the advantage of preserving local extrema and sign of the transported properties. The scheme assures solutions consistent with analytic properties of the modeled system and minimizes the need for artificial viscosity while suppressing the nonlinear instabilities of computations. The model uses a diagnostic Smagorinsky-type subgrid scale (SGS) parameterization (Deardorff, 1973) to represent the effects of the unresolved scales of motion. An efficient iterative pressure solver based on the conjugate residual approach of Smolarkiewicz and Margolin (1994) is used to compute pressure at each time step.

No-slip boundary conditions are used at the model surface and building surfaces. Free-slip boundary conditions are used at other model boundaries. Surface temperatures and sub-grid scale fluxes are updated using Monin-Obukhov similarity theory (a meteorological analogue to engineering law-of-wall functions; see Pielke, 1984). The version of the model used in this study can be run on massively parallel architectures, allowing high resolution, 3-D simulations in a comparatively short time.

2.2. *Physics Package*

A 1-D physics package is included in the model to simulate the effects of radiative heating in the atmosphere, and on building and ground surfaces. This package was adopted from a similar version presented by Smith and Kao (1996a), and has been validated extensively in Smith (1996), Smith and Kao (1996b), and Kao *et al*. (2000 a, b). The package includes the treatment of shortwave and longwave radiation, and surface fluxes of heat and moisture. Surface quantities are updated using a 5-layer surface model with specified albedo and emissivity for the surface, and specified heat capacity and thermal conductivity for each layer. Surface fluxes of heat and moisture are computed using Monin-Obukhov similarity theory.

2.3. *Longwave Radiation*

The longwave fluxes and heating rates were computed using a broadband method similar to that proposed by Sasamori (1968). This method takes into consideration absorption due to CO_2, water vapor, and ozone. The parameterization is bounded by assuming a longwave flux of 50 W m^{-2} at a height of 10 Km above sea level. In the approach, the upward and downward longwave fluxes are computed by integrating the mean absorptivity over the range of temperature from a given level at height z to the upper or lower model domain, respectively. The mean absorptivity is further parameterized using a weighted mean absorptivity, which can be conveniently expressed using algebraic expressions, which are functions of the path length. The weak overlapping absorption due to water vapor and CO_2 in the 15 μm band is treated by assuming that the resultant transmissivity is the product of the water vapor transmissivity and the CO_2 transmissivity. The current parameterization, which was originally designed by Sasamori (1968) to be used in the clear atmosphere, has been modified to account statistically for the effect of partial cloudiness. The method is similar to that proposed by Manabe and Strickler (1964). Each cloud level is assumed to behave as a blackbody radiator. The upward and downward longwave fluxes at each level are then computed by assessing the probability that longwave flux will traverse a given vertical region unimpeded by cloud. In this paper, ground and building surfaces are also treated as blackbodies.

2.4. *Shortwave Radiation*

The shortwave radiation parameterization uses a two-stream delta-eddington method to calculate the upward and downward solar flux and shortwave heating rates for each model layer. The parameterization accounts for water vapor, CO_2, and ozone. A portion of the solar spectrum is sub-divided into six water vapor absorption bands at 0.94 μm, 1.10 μm, 1.38 μm, 1.87 μm, 2.7 μm, and 3.2 μm where absorption due to water vapor is most significant. The water vapor absorption for each band is expressed as a finite weighted sum of exponentials with corresponding effective absorption coefficients. Each term in the sum then represents a pseudo-monochromatic band. The weighting factors and effective absorption coefficients for each of these bands are taken from Liou and Sasamori (1975), while the fractional solar fluxes for each band are from Liou and Wittman (1979). The remainder of the solar spectrum is divided into an additional six bands for CO_2, ozone, and radiatively inactive portions of the solar spectrum (window bands). The shortwave treatment can also account for Rayleigh scattering, and scattering do to cloud water (Slingo and Schrecker, 1982). For this study, shading due to solid obstacles such as buildings has been incorporated into the physics package. This was achieved by splitting the shortwave component of the radiative flux into a direct and diffuse component, and applying logic to shade only the direct component.

3. MODEL VALIDATION

The numerical simulations shown in this section were designed to model the dynamical flow field around a single building. In order to facilitate a fair comparison with the towing-tank data and associated numerical simulations presented in Zhang *et al*. (1996), we adopt the size of the computational domain, the prevailing wind speed, the location of tracer release, and the dimension of the cubical building from their study. These parameters were selected to ensure that the major details of the mean and turbulent flow field in the vicinity of the building, revealed by the towing-tank experiments, could be adequately modeled.

In all experiments shown in this section, we use a uniform initial prevailing wind (U_o) of 7 m s^{-1} from west to east and normal to the building surface. Buildings were cubical with dimensions set to 60 m for each side. The 3-D model domain was set to 750 m in the longitudinal direction, 350 m in the lateral direction, and 250 m in the vertical. The model resolution was set to 5 m in all directions. Time increments were selected so as not to exceed the Courant condition. This normally required a time increment of about 0.5 s or less. A continuous inert tracer release was conducted throughout each experiment. Tracer was released in a single grid cell at a height of 5 m, and a longitudinal distance of one quarter of the building length (H_b) downstream of the building surface. The tracer release rate (Q) was arbitrarily set to 1.0 Kg s^{-1}. All simulations were conducted for a period of one hour. Time-averaged fields were averaged over the last 20 minutes of simulation. This provided sufficient time for model spin-up and collection of statistics. Five numerical simulations with different Froude numbers (∞, 12, 3, 2, and 1) were conducted. No radiative effects were included in the simulations.

Figure 1 shows the comparison of the modeled cavity length (L_c) (normalized by the building height (H_b)) as a function of Froude number, with the towing-tank data and the modeled results from Zhang *et al.* (1996). L_c represents the normalized distance from the downstream edge of the building to the reattachment point at ground level along the vertical center-plane of the building. It is seen in Fig.1 that our modeled L_c is in a better agreement than Zhang *et al.* (1996) in the regime where Froude numbers are larger than 3. The secondary transition in the range of Froude numbers from 6 to 3 reported by Zhang *et al.* (1996) is not seen in our model results. On the other hand, we overestimate L_c for small Froude number in comparison with the towing-tank data. In addition, our model shows that the reattachment point is nearly independent of Froude number for Froude numbers greater than 2. This threshold Froude number is smaller than the value of 3 suggested by Snyder (1994) and Zhang *et al.* (1996). As pointed out by Zhang *et al.*, the differences between modeled reattachment lengths and tow-tank data at small Froude numbers may be attributed to the differences between atmospheric and towing-tank Reynolds numbers (Re), and the dependence of the critical Reynolds number on Froude number. While both towing-tank and modeled simulations were verified to be above the critical Reynolds number of 11,000 determined for high Froude numbers, Zhang et al. (1996) noted that "it is not obvious that the Reynolds numbers in the range of 1.3×10^4 — 3.9×10^4 in the stratified flow experiments are also above the critical Reynolds number for Re-independence at low Froude numbers".

Figure 2 shows the x-z vertical center-plane across the building for the two extreme cases, respectively, with Froude numbers of infinity (neutral) and 1 (highly stratified). The differences due to the stratification in the two cases are reflected by the size of the cavity region behind the building as well as the flow field just above the building. In the case with Froude number equal 1, the cavity circulation is considerably smaller and skewed. No reversed flow is observed at the roof of the building. One noticeable feature in Fig. 2b is the lee wave downstream of the building. This wave structure has a half wavelength of about 180 m. The modeled wavelength agrees fairly well with that computed from $\lambda = 2\pi H_b F_r$, as suggested by Snyder (1994), where λ is the wavelength and F_r is the Froude number. No similar wave structure was reported in the simulations of Zhang *et al.* (1996).

Figure 3 shows the corresponding velocity vector fields in the horizontal plane at $1/2$ the building height. The major difference between Figs. 3a and b again lies in the size of the cavity region. The reversed flows near the building are similar between the two cases. Zhang *et al*. (1996) show that the flows near the north and south sides of the building in the case of Froude number equal 1 appear to be different than the case with Froude number of infinity. This may be due to the different SGS parameterizations used. The weaker outflow shown in Fig. 3b is apparently associated with the wave motion resolved by the model.

Figure 4 shows the comparison of the modeled surface concentration, from a tracer release located $H_b/4$ downwind of the building, with the towing-tank measurements. The concentration is normalized using $\chi = CU_o H_b^2/Q$ where C is the modeled tracer concentration, and χ is the normalized concentration. χ is plotted in the lateral direction at 6.0 H_b downstream from the building. A Froude number of 3 was selected for the model run and towing-tank data. It is seen that the comparison of our modeled concentration with the towing-tank data is quite good. The bi-modal distribution shown in the results by Zhang *et al*. (1996) is probably due to a weaker flow downwind from the building near the centerline of the horizontal plane (see their Fig. 4b).

4. SIMULATED RADIATIVE EFFECTS

The numerical simulations shown in this section were designed to isolate the influence of radiative heating and shading effects on the dynamical flow field around a single building. The simulations were idealized in the following sense. The albedo, emissivity, thermal conductivity and heat capacity of the building surfaces were set to constant values of 0.3, 0.98, 0.84 W m^{-1} $^{o}K^{-1}$, and 1256.0 J Kg^{-1} $^{o}K^{-1}$. These values were also assigned to the ground surface. Sun azimuth and zenith angles at any time during the simulation were computed assuming a latitude of 39^{o} N on Julian day 180. All simulations were initiated at 0730 LST in order to provide significant shading on the western side of buildings, and moderate radiative heating.

The initial environmental potential temperature profile was set to a constant value of 300 ^{o}K. In contrast to the towing-tank simulations described in the previous section, a power law profile ($U/U_o = (z/z_o)^m$) expressing a more typically observed ambient atmospheric horizontal wind speed (U) as a function of vertical height (z) was selected, where U_o =4 m s^{-1}, m =0.16, and z_0 =360 m. The grid resolution was set to 4 m in the horizontal and vertical dimensions, with a domain size of 600 m in the longitudinal direction, 280 m in the lateral direction, and 200 m in the vertical. The building's dimensions were, accordingly, set to be 40 m for each side. A continuous inert tracer release was conducted throughout each experiment. Tracer was released in a single grid cell at a height of 4 m, and a longitudinal distance of 4 m either upstream or downstream of the building surface. The tracer release rate was again set to 1.0 Kg s^{-1}.

All simulations were conducted for a period of one hour. Time-averaged fields were averaged over the last 20 minutes of simulation. This provided sufficient time for model spin-up and collection of statistics. The results with radiative heating and shading are later compared to the case without radiation in order to determine the overall effect of radiative heating and shading. Shading effects are further determined by reversing the wind direction and changing the sun angle in the experiments.

4.1. *2-D Cases*

The 2-D experiments shown here serve two purposes: (1) they provide a base-line demonstration of the radiative heating and shadowing effects, and (2) they provide a representation of the flow around a building whose lateral extent is much longer than its longitudinal dimension. They also provide a reference for the more complex 3-D simulations shown in the next section. Figure 5 shows the potential temperature for two cases (*a* and *b*) that are identical in every respect except that the wind direction in case *b* is reversed compared to case *a*. For both cases, the shaded portion of the building is located on the left side of the building, as represented by a relatively cool region near the surface in Figs. 5a and 5b. Therefore, the only difference in terms of the physical forcings between the two cases is that the shading is upstream of the building in case *a* and downstream in case *b*.

There are several distinct differences between Figs. 5a and 5b. First, the recirculation at the upstream face of the building in case *a* is clearly enhanced compared to case *b*. This recirculation causes heat exchange so that the air immediately above the cool, shaded ground surface is significantly cooler than the air in the corresponding upstream region in case *b*. The warming at the upstream face in case *b* is, of course, caused by the radiatively heated ground. Both cases show a significant transport of heat from the rooftop, that is advected leeward of the building. This heating provides some thermal stability in case *b* that somewhat reduces the strength of the counter-rotating portion of the cavity zone.

Figures 6a and 6b show the tracer dose (the time integration of the tracer concentration over the model simulation) at one hour of simulation for cases *a* and *b*. In these runs, a continuous tracer release occurs at 4 m height, and one building length upstream from the windward face of the building. The maximum tracer dose in Fig. 6a is reduced by more than a factor of two compared to Fig. 6b as a result of the enhanced recirculation (refer to Figs. 5a, b) at the upwind face of the building. For downstream tracer releases (figures not shown), our model simulations showed only small differences in the overall tracer dose near the leeward face of the building.

4.2. *3-D Simulations*

In this section we examine the flow field and tracer transport around a single 3-D cubical building. The shading pattern is illustrated in Fig. 7a, which shows the surface potential temperature field for a wind field flowing from left to right. The shading is fixed on the west side of the building for all of the following simulations. The surface potential temperature in the shaded region is about 300 ^{o}K. Note that a subtle local minimum in the potential temperature exists about three building lengths downstream of the building (the black square). This minimum is just downstream of the stagnation point of the cavity zone flow where relatively cool in the flow field is directed downward toward the surface. This provides locally increased cooling of the surface downstream of the stagnation point. A subtle thermal effect due to the mixing influence of the horseshoe eddy is also evident in the potential temperature distribution that streams off along the lateral sides of the building.

Figures 7b and 7c show horizontal cross sections of the flow field and potential temperature at a vertical height of 4 m above the surface for two cases. For both cases, the shading at the surface is to the left side of the building as shown in Fig. 7a. But the wind direction is reversed between the two cases. There are distinct differences in the flow field in the vicinity of the building. In Fig. 7b, there is a local increase in the potential temperature of the recirculating air near the leeward face of the building. This is apparently associated with the heat transport from the ground to the air in close proximity to the heated surface as it recirculates in the cavity zone. Thermal heating of the ground and building surfaces results in an interesting surface convergence of warm air downstream of the building, as will be discussed below. In contrast, this same recirculation of air in the shaded downstream cavity zone in Fig. 7c results in slightly cooler air in this area. As discussed in the previous section for the 2-D cases, a somewhat reduced strength of the leeward circulation is seen due to the rooftop heating.

Fig. 8a shows the corresponding vertical cross section through the center of the building. In comparison with Fig. 8b, where radiative heating and shading effects are neglected, the differences in the gross features of the flow field are striking. Without the heating effects, the flow field is characterized by a fairly typical cavity zone and recirculation on the leeward face of the building. Note that, due to the 3-D configuration, the reversed flow near the windward side of the building is quite different from that shown in Fig. 5a for the 2-D case, since the flow is allowed to go around the building in the 3-D cases. Figure 8a reveals significant convergence of air within the cavity zone and beyond, resulting in substantial lofting of the air mass immediately downstream of the building. This interesting dynamic appears to be the result of a combination of effects that can be attributed to thermal heating of the ground and building roof, and vortex circulation associated with the horseshoe eddy along the lateral sides of the building. Shading did not seem to play a central role in the observed thermally induced lofting downstream from the building (Fig. 8a), since its cooling effects did not strongly affect the cavity zone, as seen from Figs. 7b and c. The resultant vertical lofting, and associated lateral circulations generated in the cavity zone will be discussed in more detail later in this section.

We now examine asymmetries induced in the flow field in the vicinity of a building due to shading that is laterally situated with respect to the wind flow. Figure 9a shows the shading pattern and resulting surface potential temperature distribution imposed on a second series of numerical experiments, where the model horizontal configuration is changed to a different orientation, as shown in Fig. 9. In these experiments, the shading is oriented to the west (left) side of the building, while the winds are southerly. The surface heating pattern is similar in many respects to those shown in Fig. 7a. But asymmetry of the flow field, induced by the shading pattern, is clearly evident in the Fig. 9b. The left, leeward corner of the building in Fig. 9a is cooler than the corresponding area on the right. This is clearly due to the air flowing from the cool, shaded region. The effect of the shading on the flow field and tracer transport at 4 m above the ground surface is illustrated in Fig. 9b. Tracer is released 4 m from the building downwind at the centerline. A significant asymmetric, lateral circulation is induced on the leeward side of the building as relatively cool air from the shaded region (left) introduces more west-to-east pressure gradient force. This results in the transport of the tracer being offset toward the right edge of the building.

The thermally induced flow, discussed above, is more clearly illustrated in Figs. 10a and 10b which show, respectively, the cross sections of potential temperature and tracer dose in a plane 1/2 building length behind the leeward surface of the building. The wind field vectors and potential temperature field shown in Fig. 10a illustrate the lateral vortices associated with the horseshoe eddy on either side of the building. These vortices draw relatively cooler air into the cavity zone. This air is displaced upward, and is entrained into relatively warm, lateral vortices emanating at roof- top. The warm air at the rooftop level and above, shown in Fig. 9a, is transported primarily from the building roof, as evidenced by the stream flow above the roof and downstream, shown in Fig. 8a. Note that relatively cool air, which is directly influenced by the shaded region, is drawn from the left side of the building,. This, in turn, directs the upward motion and tracer dose distribution toward the right edge of the building, as seen in Fig. 10b. The interaction of circulating air due to these vortices, and thermal heating of the ground and roof surfaces, results in a net convergence and lofting of warm air immediately downstream of the building.

Figures 11a and 11b show the thermal distribution, flow field, and tracer dose further downstream (2 building lengths) of the leeward building surface. At this point and further downwind of the building, any effect due to the shadowing on the left side of the building seems to be greatly diminished, as evidenced by the more symmetric flow pattern. In Fig. 11a the lateral, counter-rotating flow at either side of the building due to the horseshoe eddies is apparent. The combination of surface heating at rooftop, and rising air warmed by contact with the ground surface produces counter-rotating lateral vortices at approximately the rooftop level. As shown in Fig. 11b, the flow pattern exhibited by Fig. 11a results in much of the tracer being lofted above rooftop level in the two counter-rotating lateral vortices. Another much smaller local maximum in the tracer dose results near the surface. This pattern contrasts with the more familiar flow field and tracer dose pattern (Fig. 11c) for flow around a building without imposed thermal heating and shading effects. In this case, the maximum tracer dose is located near the surface with a slightly bimodal distribution along the leeward side of the building. The concentrations decrease monotonically up, and outward from these maxima.

In summary, two effects of radiative heating and shading are observed. The first is a pronounced tendency for warm air in the cavity zone to uplift, resulting in lofting of the air mass and tracer downwind of the building. The second, lesser effect, is due primarily to the shading location, which alters the flow pattern in the vicinity of the shaded region by inducing secondary vortices near the building. These two effects can have a dramatic influence on the overall tracer transport around a cubical building.

5. CONCLUDING REMARKS

The main goal of this paper is to examine the effects of radiative heating and associated shading on the flow field around an isolated cubical building. We found no corresponding field experiment data with which to compare the results of our radiative heating and shading simulations. Non-the-less, the ability of the model to capture many flow characteristics observed in corresponding towing-tank data lends credibility to the current study. These flow characteristics include the surface tracer concentrations, the variation of the flow reattachment point as a function of Froude number, and the wavelength of the simulated flows in the low Froude number regime.

Our simulations demonstrate that radiative heating, including the effects of shading, can significantly influence the overall flow field in the vicinity of a building. The resulting evolution of a tracer released in the vicinity of a building can, therefore, also depend significantly on these influences. Our 2-D simulations show that shading near the windward face of the building can enhance the recirculation upstream of the building. On the other hand, the shading near the leeward face of the building can slightly reduce the strength of the counter circulation in the cavity zone downstream of the building due to the thermal stability induced by the rooftop heating.

The 3-D simulations of the radiative effects reveal significant convergence of air within the cavity zone and beyond, resulting in substantial lofting of the air mass immediately downstream of the building. This dynamic is the result of the combination of effects that can be attributed to thermal heating of the ground and building roof, and vortex circulation associated with the horseshoe eddy along the lateral sides of the building. Namely, warm air near the surface tends to be inducted into the cavity flow. This results in the formation of two counter-rotating vortices at about roof top level, and a net upward lofting of the air mass downstream of the building.

The shading effects in the 3-D simulations are considerably more subtle and complicated. Shading upstream of the building seems to play a secondary role in the observed thermally induced lofting downstream from the building, since its cooling effects do not affect the cavity zone as directly as the overall thermal heating of the ground and building. Shading downstream of a cubical building tends to somewhat diminish the cavity circulation and counter circulation near the leeward wall of the building. Lateral shading, however, helps to induce lateral vortices near the leeward building face that can significantly skew the flow pattern and tracer dose distribution.

Acknowledgments - This research was funded by the U. S. Department of Energy (DOE) Nonproliferation Program. Some of the simulations reported in this paper were conducted using the resources of the Advanced Computing Laboratory supercomputing facilities, Los Alamos National

Laboratory, Los Alamos, New Mexico. We are also grateful to Dr. M. Brown of TSA-4, Los Alamos National Laboratory for his help in reviewing our original manuscript.

REFERENCES

Dawson, P., Stock, D. E, Lamb, B., 1991. The numerical simulation of airflow and dispersion in three-dimensional atmospheric recirculation zones. J. Appl. Meteor., 30, 1005-1024.

Deardorff, J. W., 1973. Subgrid length-scales for large-eddy simulation of stratified turbulence. J. Fluids Eng., 95, 429-438.

Guenther A., Lamb, B., Stock, D., 1990. Three-dimensional numerical simulation of plume downwash with a k-epsilon turbulence model. J. Appl. Meteorl., 29, 633-643.

Kao, C.-Y. J., Hang, Y. H., Reisner, J. M., Smith, W. S., 2000a. Test of the volume-of-fluid method on simulations of marine boundary layer clouds. Mon. Wea. Rev., 128, 1960-1970.

Kao, C.-Y. J., Hang, Y. H., Cooper, D. I., Eichinger, W. E., Smith, W. S., Reisner, J. M., 2000b. High-resolution modeling of LIDAR data: Mechanisms governing surface water vapor variability during SALSA. Agri. and Forest Meteorol., (in press).

Liou, K.-N., Sasamori, T., 1975. On the transfer of solar radiation in aerosol atmospheres. *J. Atmos. Sci.,* 32, 2166-2177.

Liou, K.-N., Wittman, G. D., 1979. Parameterization of radiative properties of clouds. *J. Atmos. Sci.,* 7, 1261-1273.

Manabe, S., Strickler, R. F., 1964. Thermal equilibrium of the atmosphere with a convective adjustment. J. Atmos. Sci., 21, 361-385.

Mestayer, P. G., Moussiopoulos, N., Brebbia, C. A., 1995. Simulation of the wall temperature influence on flows and dispersion within street canyons. 3rd International Conference on Air Pollution, Porto Carras, Greece, Computational Mechanics, 1, 109-116.

Murakami, S., Mochida, A., Hibi, K., 1987. 3-Dimensional numerical simulation of air-flow around a cubic model by means of large eddy simulation. J. Wind Eng. Ind. Aero., 25, 291-305.

Pielke, R. A., 1984. Mesoscale Meteorological Modeling. Academic Press, New York. Chapt. 7

Reisner, J. M., Smith, W. S., Bossert, J. E., Winterkamp, J. L., 1998. Tracer modeling in an urban environment. Second Urban Environment Symposium, Albuquerque, NM., Am. Meteor. Soc., 22-25.

Sasamori, T., 1968. The radiative cooling calculation for application to general circulation experiments. J. Appl. Meteor., 7, 721-729.

Sini, J.-F., Anquetin, S., Mestayer, P. G., 1996. Pollutant dispersion and thermal effects in urban street canyons. Atmos. Env., 30, 2659-2677.

Slingo, A., Schrecker, H. M., 1982. On the shortwave radiative properties of stratiform clouds. Quart. J. Roy. Meteor. Soc., 108, 407-426.

Smith, W. S., 1994. A study of the cloud/radiation interaction using a second order turbulence closure radiative/convective model. Ph.D. dissertation, New Mexico State University, 283 pp.

Smith, W. S., Kao, C.-Y. J., 1996a. Numerical simulations of observed arctic stratus clouds using a second order turbulence closure model. J. App. Met., 35, 47-59.

Smith, W. S., Kao, C.-Y. J., 1996b. Numerical simulations of the marine stratocumulus-capped boundary layer and its diurnal variation. Mon. Wea. Rev., 124, 1803-1816.

Smolarkiewicz, P. K., Margolin, L. G., 1993. On forward-in-time differencing for fluids: Extension to curvilinear framework. Mon. Wea. Rev., 121, 1847-1859.

Smolarkiewicz, P. K., Margolin, L. G., 1994. Variational solver for elliptic problems in atmospheric flows. Appl. Math. and Comp. Sci., 4, 527-551.

Smolarkiewicz, P. K., Margolin, L. G., 1998. A finite difference solver for geophysical flows. J. Comp. Phys., 140, 459-480.

Snyder, W. H., 1994. Some observations of the influence of stratification on diffusion in building wakes. In Stably Stratified Flows: Flow and Dispersion over Topography (edited by Castro I. P. and Rockliff N. J.), Clarendon Press, Oxford, pp. 301-324.

Thompson, R. S., Lombardi, D. J., 1977. Dispersion of rooftop emission from isolated buildings: A wind tunnel study. EPA-600/4-77-066, United States Environmental Protection Agency, 36 pp.

Trent S. D., Eyler, L. L., 1987. A three-dimensional time-dependent computer program for hydrothermal analysis. Numerical methods and input instruction, Vol.1, PNL-4348. Pacific Northwest Laboratory, Battelle, Washington.

Zhang, Y. Q., 1993. Numerical Simulation of flow and dispersion round buildings. Ph.D. dissertation, North Carolina State University, 146 pp.

Zhang, Y. Q., Arya S. P., Snyder, W. H., 1996. A comparison of numerical and physical modeling of stable atmospheric flow and dispersion around a cubical building. Atm. Env., 30, 1327-1345.

Figure Legends

Figure 1. Normalized reattachment length (L_c) versus Froude number. Circles and solid line represent modeled results. Square symbols with dotted lines are from TEMPEST simulation of Zhang *et al.* (1996). Solid triangles represent tow-tank data (also from Zhang *et al*., 1996).

Figure 2. Wind vectors for vertical cross section along building center-line. (a) Froude number=∞. (b) Froude number=1.0.

Figure 3. Wind vectors for horizontal cross section along building center-line. (a) Froude number=∞. (b) Froude number=1.0.

Figure 4. Modeled normalized concentration at $6H_b$ downstream of leeward side of building, versus tow-tank data and corresponding TEMPEST simulation (from Zhang *et al*., 1996). Symbols represent different, but identical tows. Dotted line is concentration reported by Zhang *et al*. (1996) for TEMPEST model simulation. Froude number is 3.0.

Figure 5. Mean potential temperature field (^{o}K) for (a) case *a*: wind flowing from left to right, (b) case *b*: wind flowing from right to left. In each case, the shadowed portion of the domain extends approximately 50 m immediately to the right of the building. (Wind vectors at the upwind face of each building are white, and locally doubled in length, to help clarify the strength and direction of the flow field).

Figure 6. Tracer dose at 1 hour of simulation corresponding to Fig. 5 with tracer release upstream of the leeward building face. Dose is expressed in units per m^{-3}. 600 units-m^{-3} dose iso-surface is contoured for each case to illustrate the plume dispersion pattern upwind of the building.

Figure 7. (a) Horizontal cross section of surface potential temperature (^oK). Surface heating pattern shows shading on left side of building. (b) Mean flow field and potential temperature pattern 4 m above ground level. Wind is from left to right. (c) Same as (b) except wind is from right to left.

Figure 8. Vertical cross section of mean flow field (vectors) and potential temperature (^oK) along longitudinal centerline of the modeled building. Wind direction is left to right. (b) Corresponding wind vectors for similar case without radiative heating or shading.

Figure 9. (a) Mean surface potential temperature pattern with shading oriented laterally with respect to the mean flow (top to bottom). (b) Tracer dose (units-m^{-3}) at 1 hour of simulation. Wind direction is from bottom to top.

Figure 10. Vertical cross section $1/2$ building length downwind of leeward building surface. (a) Mean flow field (vectors) and potential temperature (^oK). (b) Corresponding tracer dose (units-m^{-3}) pattern at one hour of simulation.

Figure 11. Vertical cross section two building lengths downwind of leeward building surface. (a) Mean flow field (vectors) and potential temperature (^oK). (b) Corresponding tracer dose (units-m^{-3})

pattern. (c) Mean flow field (vectors) and tracer dose (units-m^{-3}) pattern at 1 hour of simulation, no radiative heating.

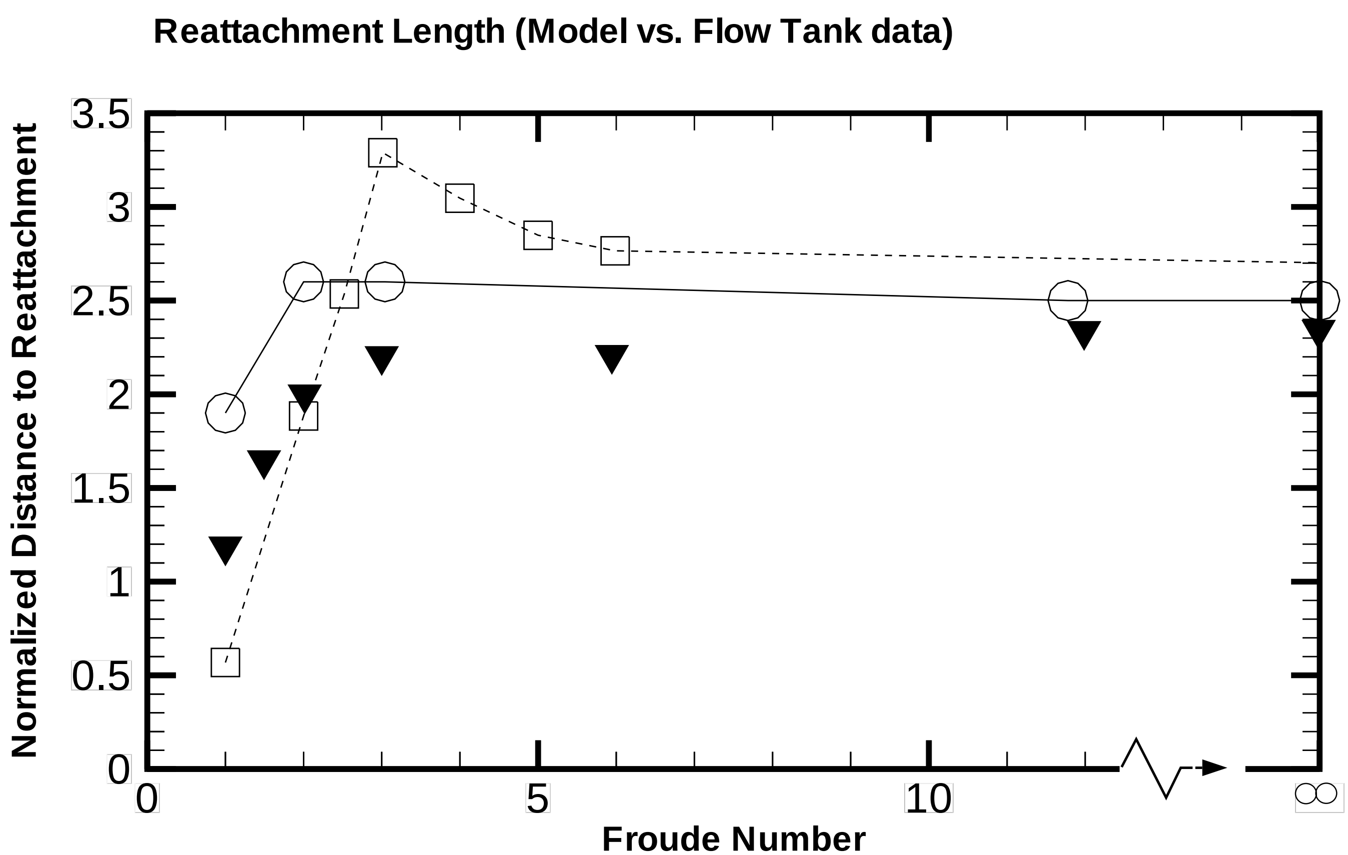

Reattachment Length (Model vs. Flow Tank data)
Normalized Distance to Reattachment
3.5
3
2.5
2
1.5
1
0.5
0
0
5
10
∞
Froude Number

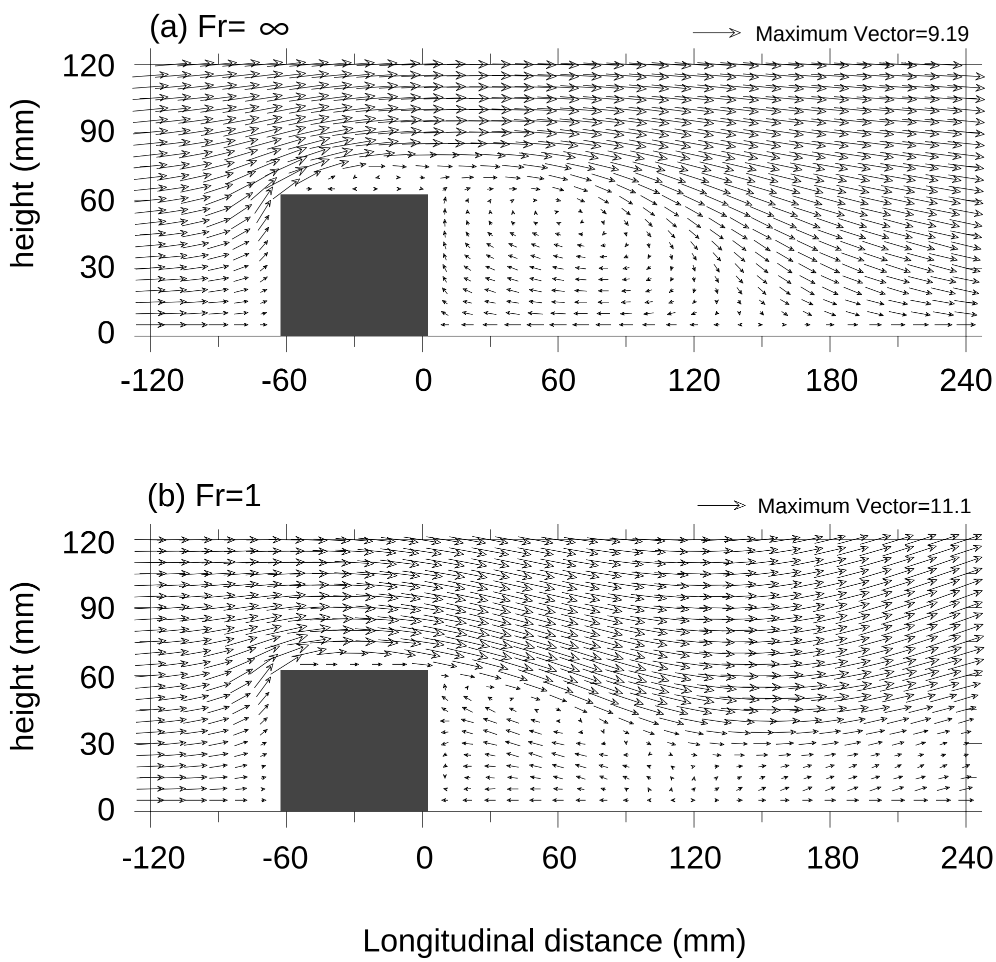

(a) Fr= ∞
Maximum Vector=9.19
height (mm)
120
90
60
30
0
-120
-60
0
60
120
180
240
(b) Fr=1
Maximum Vector=11.1
height (mm)
120
90
60
30
0
-120
-60
0
60
120
180
240
Longitudinal distance (mm)

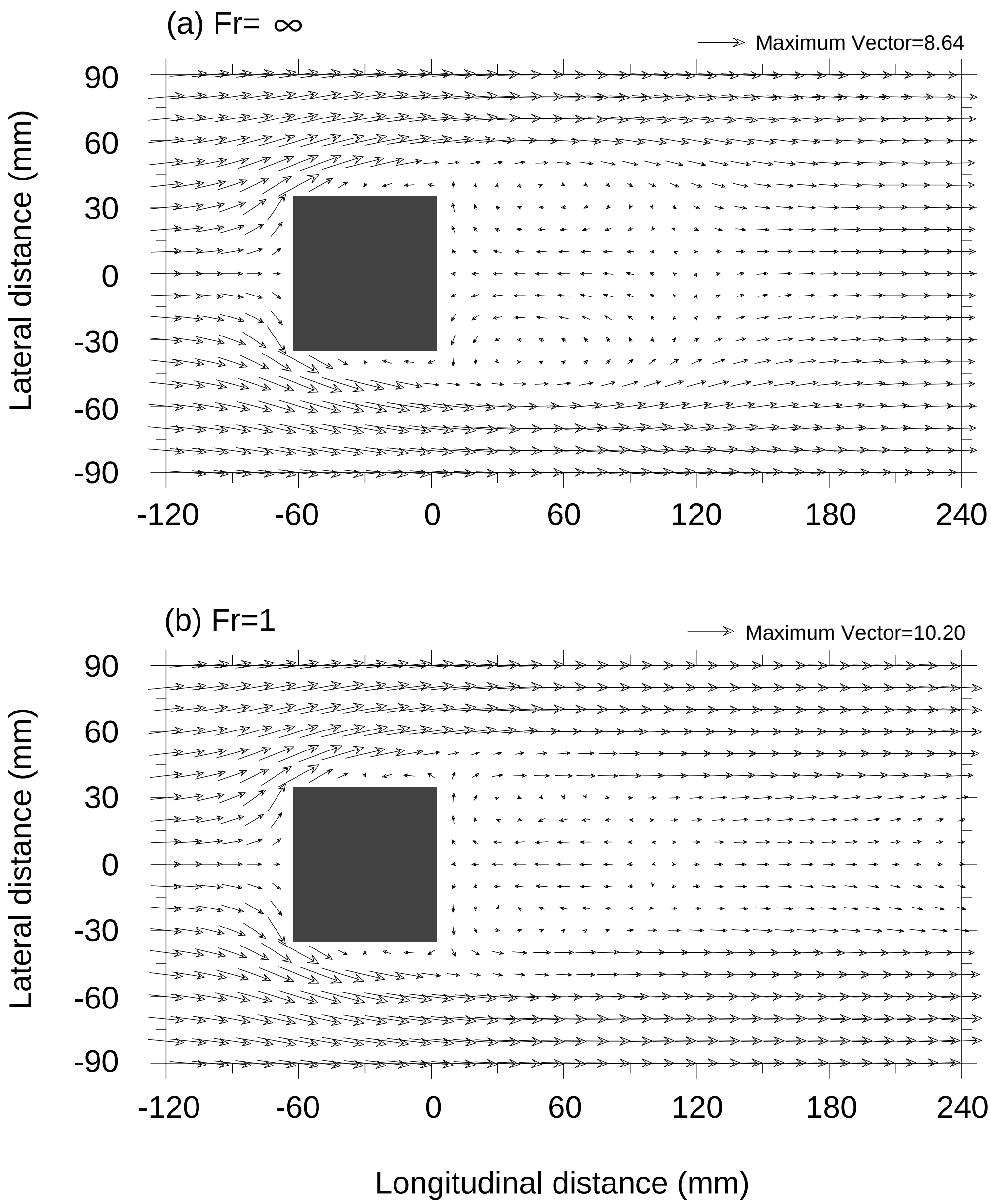
(a) Fr= ∞
Maximum Vector=8.64
90
60
30
0
-30
-60
-90
Lateral distance (mm)
-120
-60
0
60
120
180
240
(b) Fr=1
Maximum Vector=10.20
90
60
30
0
-30
-60
-90
Lateral distance (mm)
-120
-60
0
60
120
180
240
Longitudinal distance (mm)

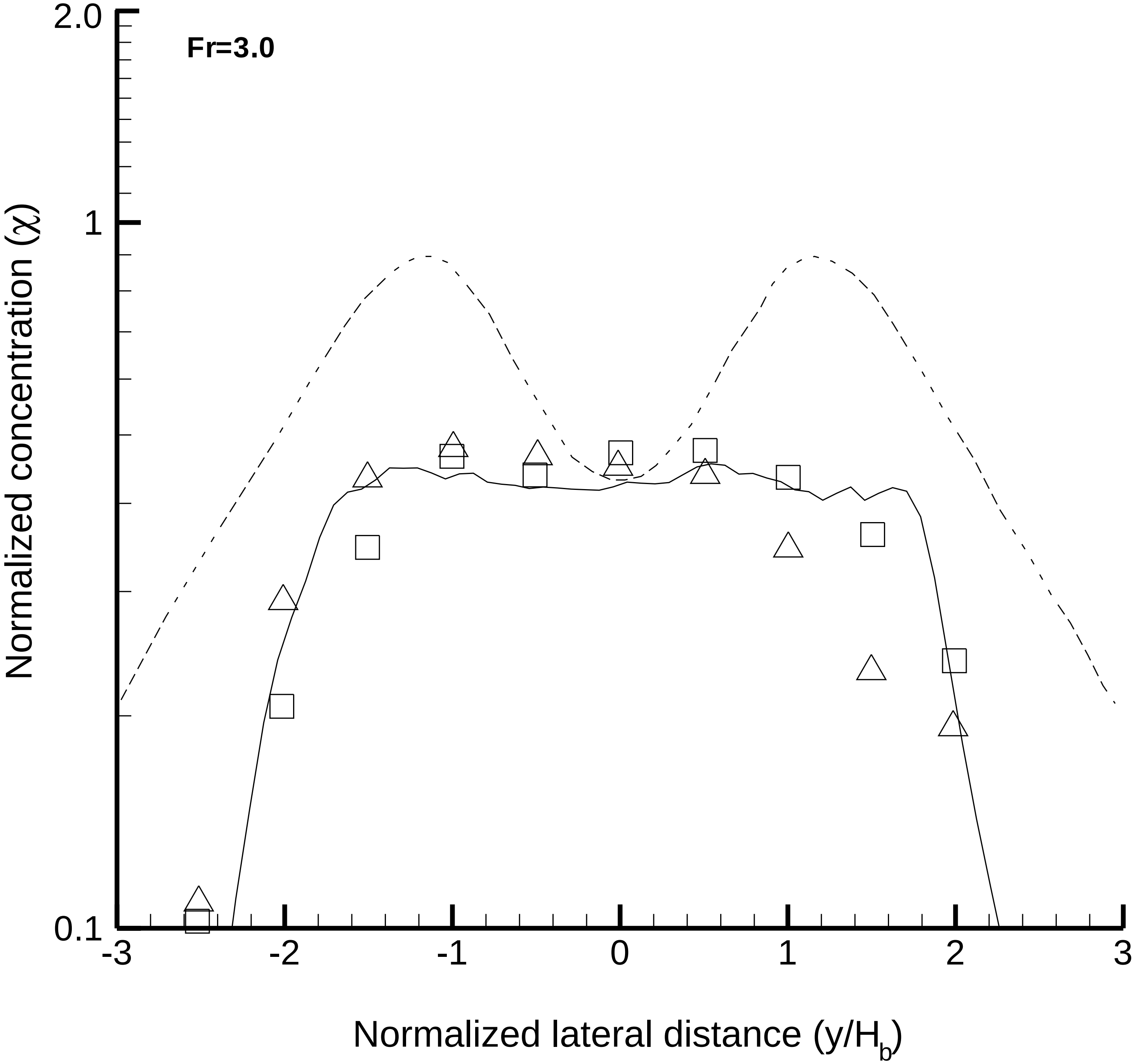

Fr=3.0
2.0
1
0.1
-3
-2
-1
0
1
2
3
Normalized concentration (χ)
Normalized lateral distance (y/H_b)

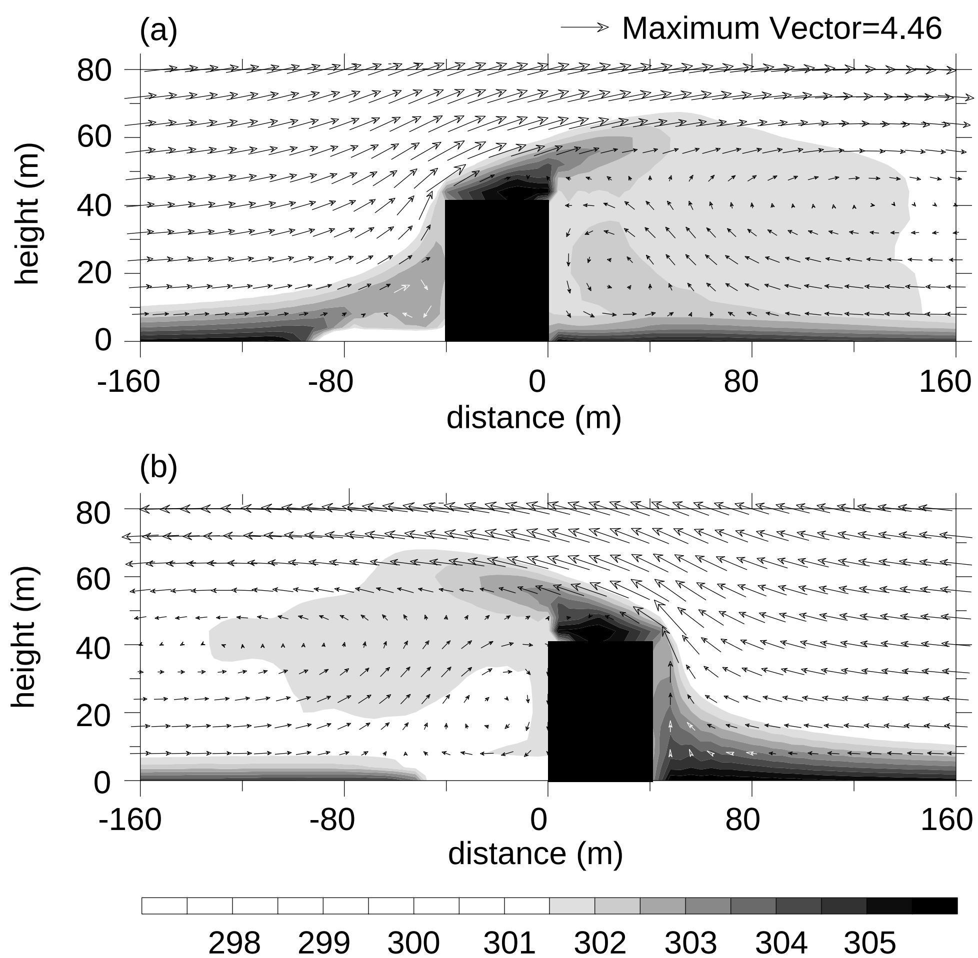
(a)
Maximum Vector=4.46
height (m)
80
60
40
20
0
-160
-80
0
80
160
distance (m)
(b)
height (m)
80
60
40
20
0
-160
-80
0
80
160
distance (m)
298
299
300
301
302
303
304
305

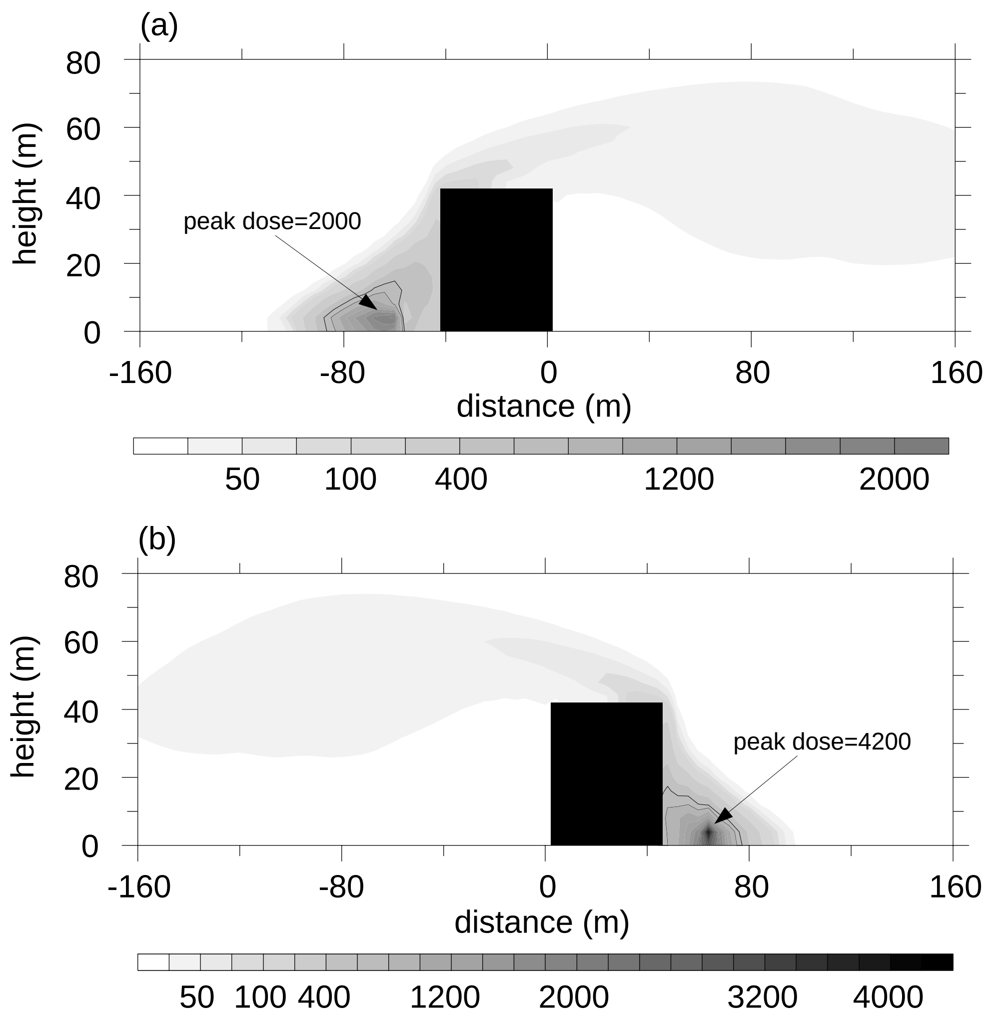

(a)
peak dose=2000
height (m)
distance (m)
50
100
400
1200
2000
(b)
peak dose=4200
height (m)
distance (m)
50
100
400
1200
2000
3200
4000

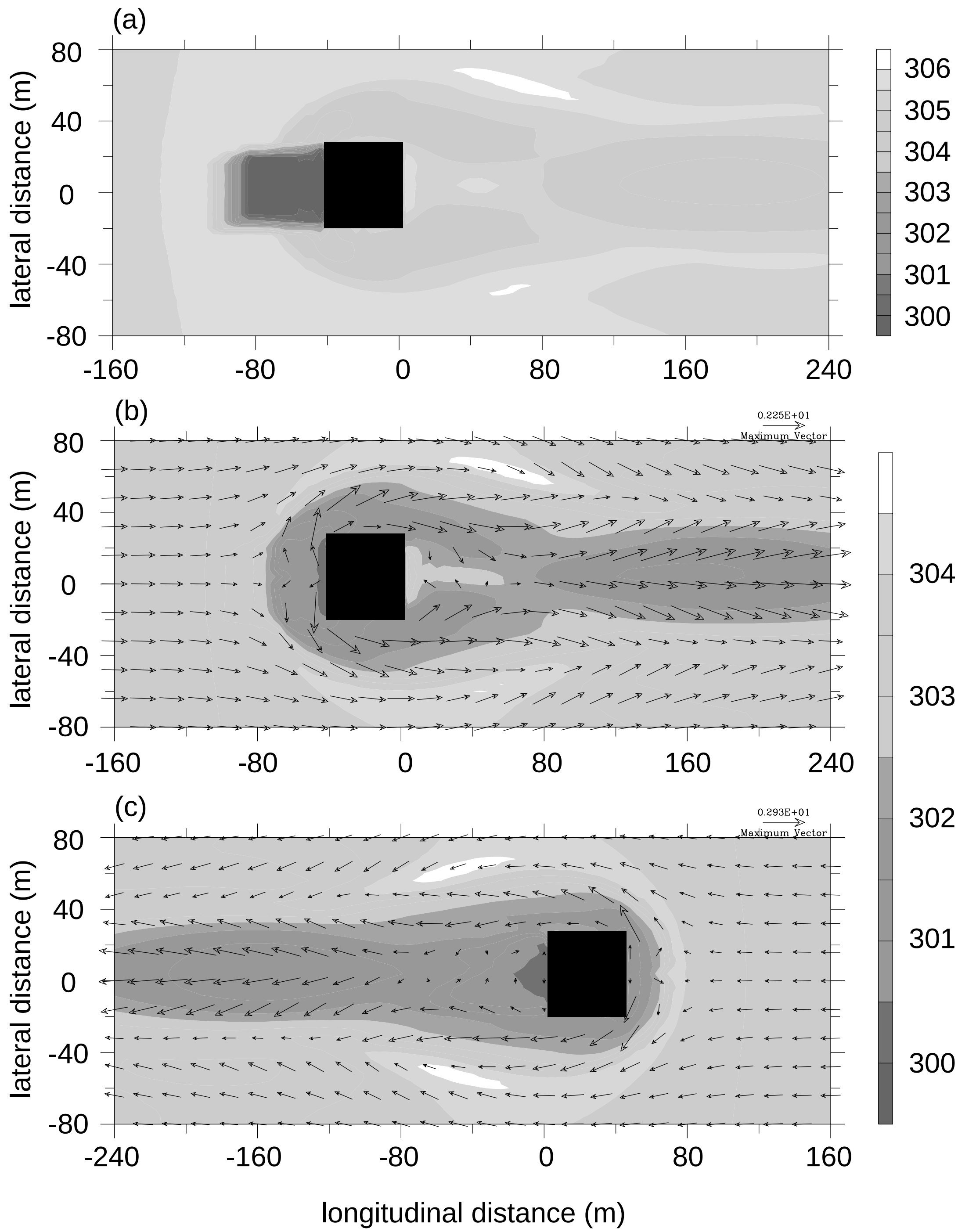

(a)
(b)
(c)
lateral distance (m)
longitudinal distance (m)
306
305
304
303
302
301
300
0.225E+01
Maximum Vector
0.293E+01
Maximum Vector

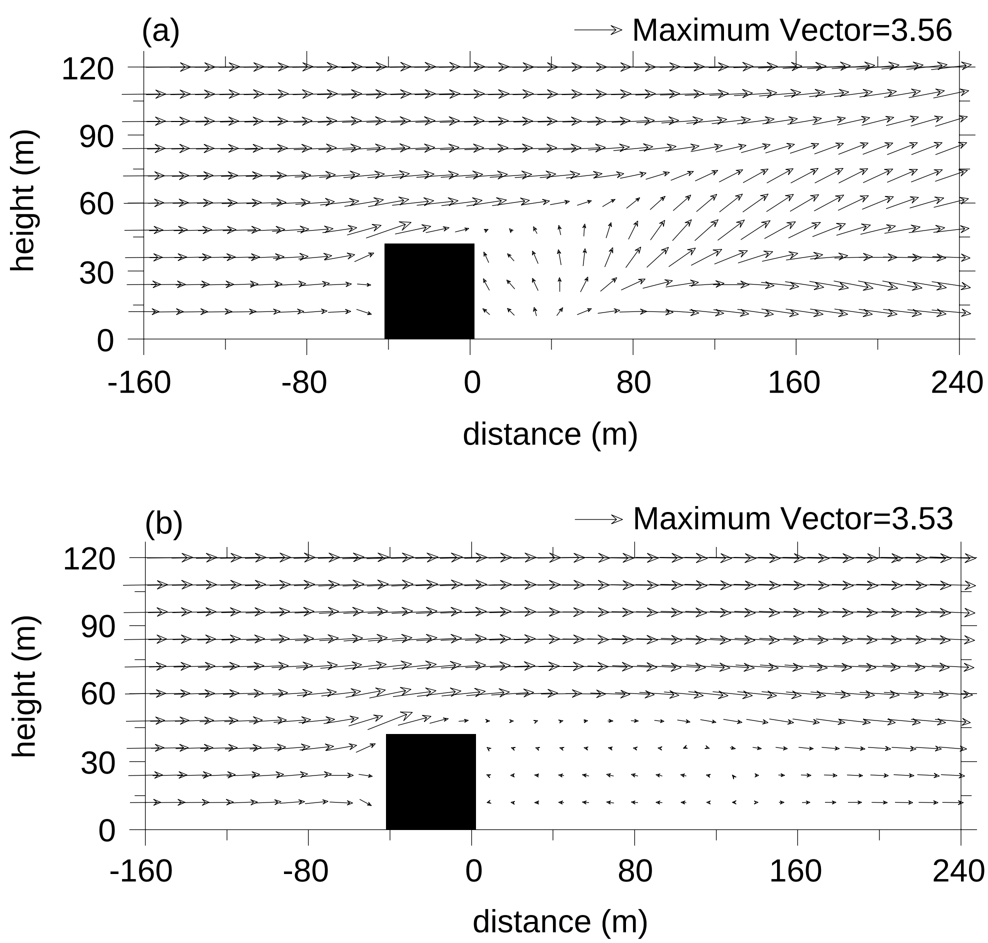
(a)
Maximum Vector=3.56
height (m)
120
90
60
30
0
-160
-80
0
80
160
240
distance (m)
(b)
Maximum Vector=3.53
height (m)
120
90
60
30
0
-160
-80
0
80
160
240
distance (m)

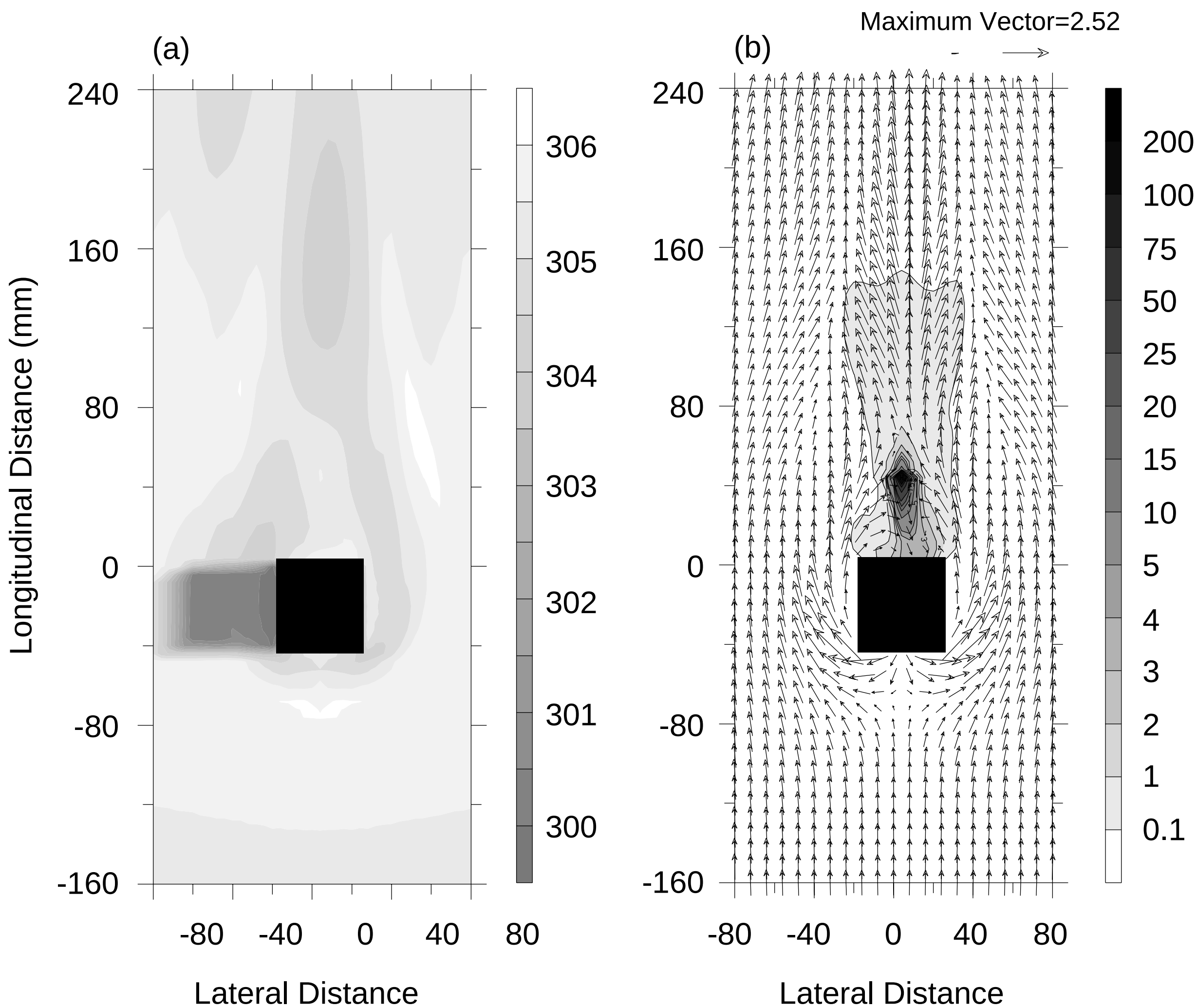
(a)
(b)
Maximum Vector=2.52
Longitudinal Distance (mm)
240
160
80
0
-80
-160
-80
-40
0
40
80
Lateral Distance
306
305
304
303
302
301
300
200
100
75
50
25
20
15
10
5
4
3
2
1
0.1

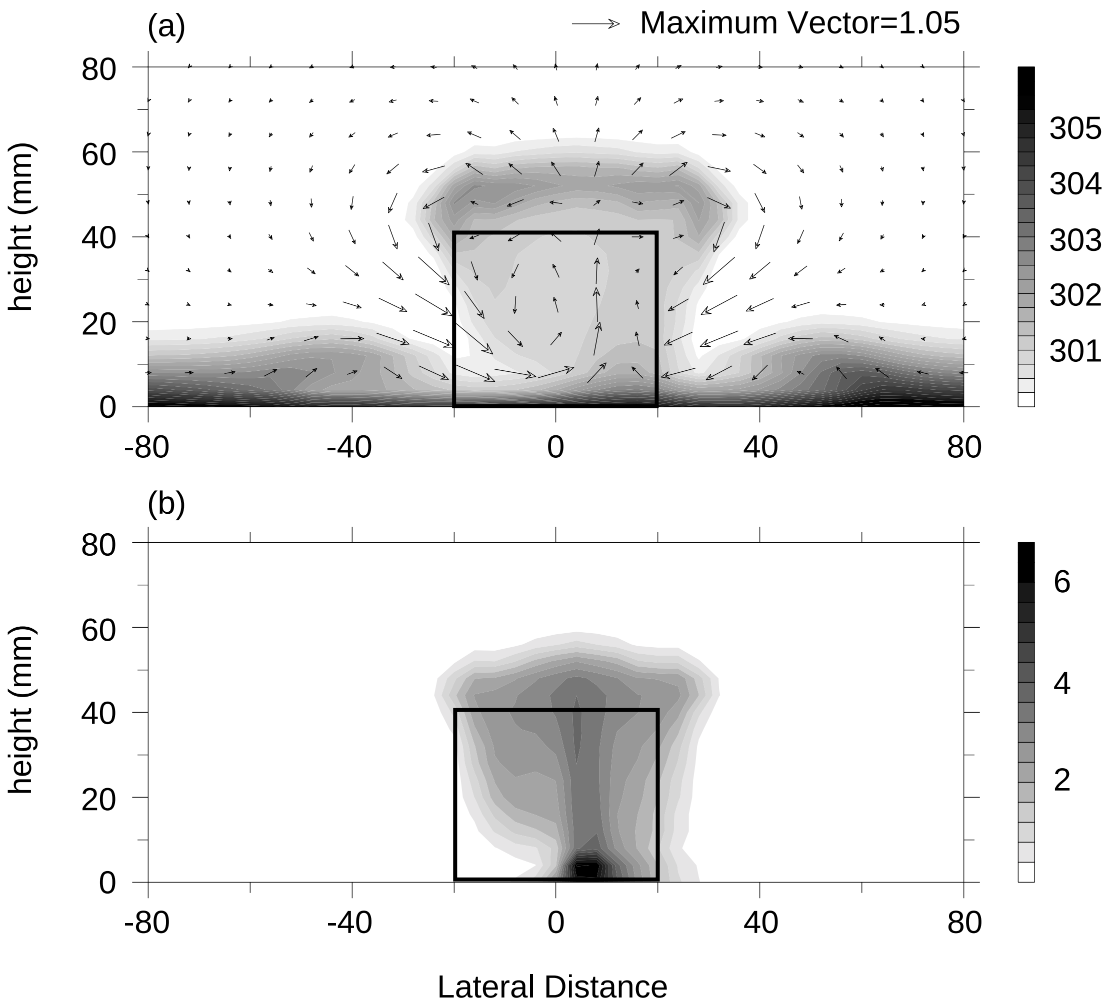

(a)
Maximum Vector=1.05
height (mm)
80
60
40
20
0
-80
-40
0
40
80
305
304
303
302
301
(b)
height (mm)
80
60
40
20
0
-80
-40
0
40
80
6
4
2
Lateral Distance

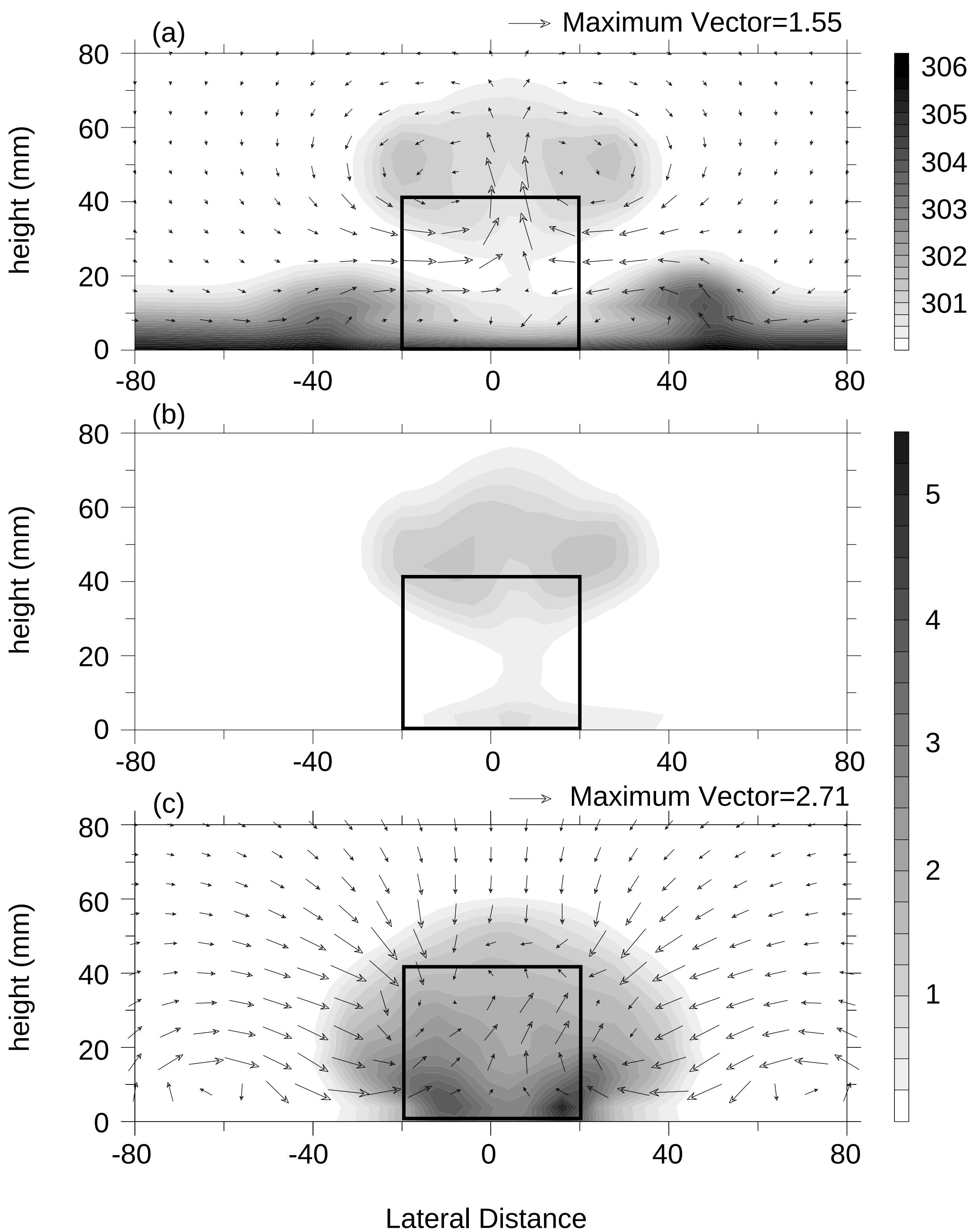
(a)
Maximum Vector=1.55
height (mm)
0
20
40
60
80
-80
-40
0
40
80
306
305
304
303
302
301
(b)
height (mm)
5
4
3
2
1
(c)
Maximum Vector=2.71
height (mm)
Lateral Distance